



# Multiple instance ensembling for paranasal anomaly classification in the maxillary sinus

Debayan Bhattacharya<sup>1,2</sup> · Finn Behrendt<sup>1</sup> · Benjamin Tobias Becker<sup>2</sup> · Dirk Beyersdorff<sup>3</sup> · Elina Petersen<sup>4</sup> · Marvin Petersen<sup>5</sup> · Bastian Cheng<sup>5</sup> · Dennis Eggert<sup>2</sup> · Christian Betz<sup>2</sup> · Anna Sophie Hoffmann<sup>2</sup> · Alexander Schlaefer<sup>1</sup>

Received: 12 January 2023 / Accepted: 27 June 2023  
© The Author(s) 2023

## Abstract

**Purpose** Paranasal anomalies are commonly discovered during routine radiological screenings and can present with a wide range of morphological features. This diversity can make it difficult for convolutional neural networks (CNNs) to accurately classify these anomalies, especially when working with limited datasets. Additionally, current approaches to paranasal anomaly classification are constrained to identifying a single anomaly at a time. These challenges necessitate the need for further research and development in this area.

**Methods** We investigate the feasibility of using a 3D convolutional neural network (CNN) to classify healthy maxillary sinuses (MS) and MS with polyps or cysts. The task of accurately localizing the relevant MS volume within larger head and neck Magnetic Resonance Imaging (MRI) scans can be difficult, but we develop a strategy which includes the use of a novel sampling technique that not only effectively localizes the relevant MS volume, but also increases the size of the training dataset and improves classification results. Additionally, we employ a Multiple Instance Ensembling (MIE) prediction method to further boost classification performance.

**Results** With sampling and MIE, we observe that there is consistent improvement in classification performance of all 3D ResNet and 3D DenseNet architecture with an average AUPRC percentage increase of  $21.86 \pm 11.92\%$  and  $4.27 \pm 5.04\%$  by sampling and  $28.86 \pm 12.80\%$  and  $9.85 \pm 4.02\%$  by sampling and MIE, respectively.

**Conclusion** Sampling and MIE can be effective techniques to improve the generalizability of CNNs for paranasal anomaly classification. We demonstrate the feasibility of classifying anomalies in the MS. We propose a data enlarging strategy through sampling alongside a novel MIE strategy that proves to be beneficial for paranasal anomaly classification in the MS.

**Keywords** Paranasal anomaly · Maxillary sinus · CNN · Classification

Anna Sophie Hoffmann and Alexander Schlaefer have equally contributed to this work.

✉ Debayan Bhattacharya  
debayan.bhattacharya@tuhh.de; d.bhattacharya@uke.de

<sup>1</sup> Institute of Medical Technology and Intelligent Systems, Technische Universität Hamburg, Hamburg, Germany

<sup>2</sup> Department of Otorhinolaryngology, Head and Neck Surgery and Oncology, University Medical Center Hamburg-Eppendorf, Hamburg, Germany

<sup>3</sup> Clinic and Polyclinic for Diagnostic and Interventional Radiology and Nuclear Medicine, University Medical Center Hamburg-Eppendorf, Hamburg, Germany

<sup>4</sup> Population Health Research Department, University Heart and Vascular Center, University Medical Center Hamburg-Eppendorf, Hamburg, Germany

## Introduction

Paranasal sinuses, located within specific bones, are prone to pathologies like retention cysts and polyps [1–3]. These anomalies, although often incidental, pose challenges for healthcare professionals, as they are unrelated to the patient's primary clinical indications [4]. Multiple studies emphasize the importance of understanding and addressing the prevalence of these paranasal anomalies in the general population [5–9].

Accurate diagnosis of paranasal inflammations is crucial for effective patient care, with medical professionals relying

<sup>5</sup> Clinic and Polyclinic for Neurology, University Medical Center Hamburg-Eppendorf, Hamburg, Germany

on CT and MRI scans to assess the extent of these conditions in the head and neck area [10]. 3D information is essential for identifying paranasal anomalies correctly, as misdiagnosis can lead to patient distress and increased healthcare costs [11]. A retrospective study found misdiagnoses of inverted papillomas and malignant tumors as nasal polyps in a significant percentage of cases [12]. Deep learning (DL) methods offer potential for improving diagnostic accuracy and reducing clinicians' workload, but the highly variable anatomy of paranasal sinuses necessitates cautious consideration when applying these techniques for reliable and accurate diagnoses [13].

DL technologies have shown significant advancements in anomaly detection, particularly in computer vision [14] and medical imaging analysis [15]. CNNs have proven effective in paranasal pathology screening, sinusitis classification, and tumor subtype differentiation. Existing studies typically follow a two-stage approach of localizing sinuses and then classifying them. For instance, one study cropped X-rays and classified anomalies [16], but failed to classify left and right MS anomalies separately. Another study segmented Computed Tomography (CT) images and classified anomalies [17], necessitating pixel-level annotations for localization. A different approach involved using a CNN to detect key slices in CT images containing MS volumes and then classifying MS anomalies [18]. However, two-stage methods relying on specialized annotations for localization and classification pose challenges in terms of increased clinician workload and limited generalization to diverse datasets.

Our proposed end-to-end approach is a non-DL solution for localizing MS volumes and a DL method for classifying MS anomalies. By employing a unique localization strategy using Gaussian sampling of centroid coordinates, we significantly expand the dataset and extract multiple overlapping instances of the MS. Leveraging a 3D CNN in our MIE prediction approach, we achieve boosted classification performance for these volumes. Through rigorous experimentation involving popular DenseNet and ResNet architectures, we ascertain the optimal MS volume size for achieving superior classification performance. Our comprehensive pipeline proves to be advantageous for accurate MS anomaly classification, providing a promising alternative to DL-based methods.

## Methods

**Dataset:** as part of the Hamburg City Health Study (HCHS) [19], cMRIs of participants (45–74 years) were recorded for neuroradiological assessment. These scans were obtained at the University Medical Center Hamburg-Eppendorf and feature fluid attenuated inversion recovery (FLAIR) sequences in the NIfTI format. The dataset comprises 299 patients, with

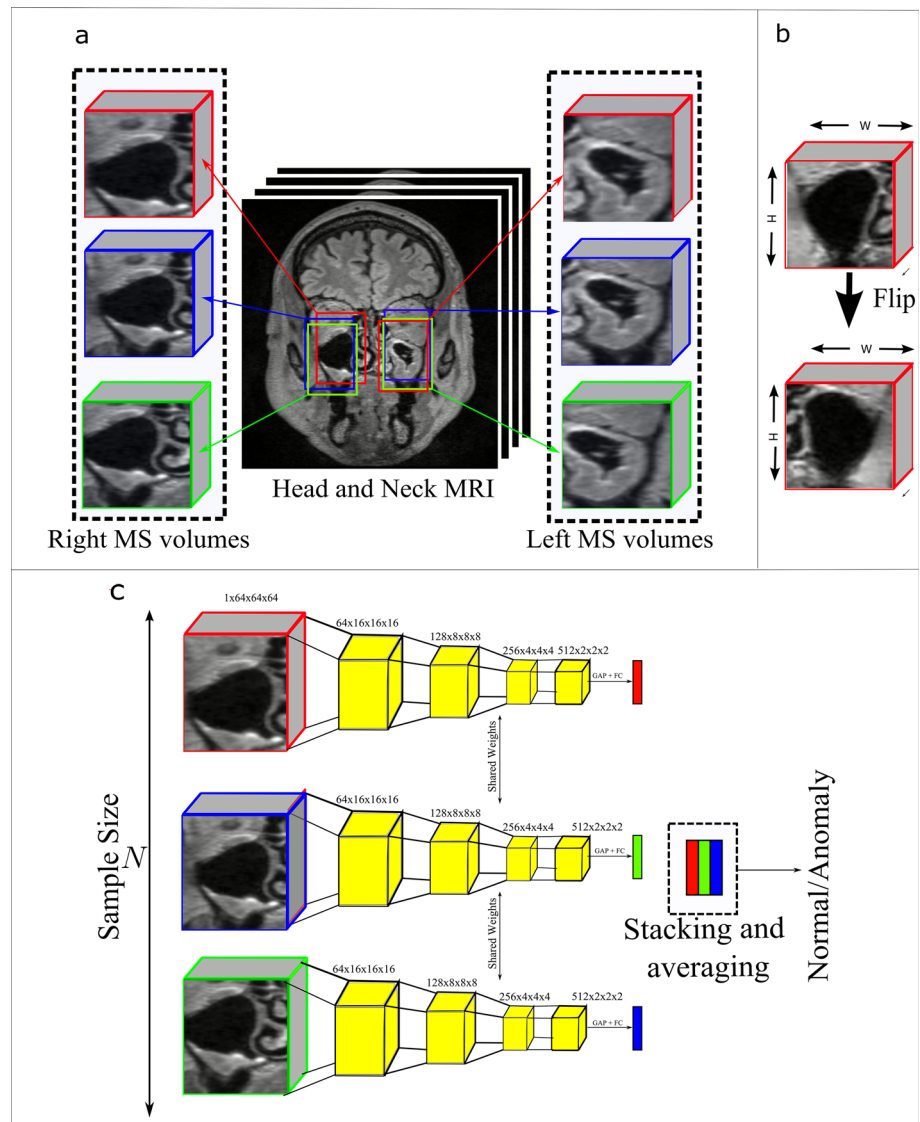
174 exhibiting healthy left and right MS and 125 exhibiting at least one MS having a polyp or cyst pathology. The diagnoses were confirmed by two ear, nose, and throat (ENT) surgeons and one ENT specialized radiologist. The anomalies under consideration in this study include polyps and cysts. MS exhibiting these anomalies are grouped into “anomalous” class and MS without these anomalies are grouped into “normal” class.

**Dataset preprocessing and MS volume extraction:** each MRI in the study has a resolution of  $173 \times 319 \times 319$  voxels, with a voxel size of  $0.53 \times 0.75 \times 0.75$  mm. To ensure consistency across all of the head and neck MRI scans in our study, we apply a process of rigid registration using Dipy library [20]. This involves selecting one MRI as a fixed volume and registering other MRIs with respect to the fixed volume.

To increase the size of the dataset and be able to use multiple instances of MS volumes for our ensemble prediction, we extracted multiple MS volumes of left and right MS from individual head and neck MRI scans. This was done by manually recording the centroid locations of the left and right MS of 20 patients, and using these coordinates to compute the mean and standard deviation of the centroid locations. These values are denoted as  $\mu(x)$ ,  $\mu(y)$ ,  $\mu(z)$  and  $\sigma(x)$ ,  $\sigma(y)$ ,  $\sigma(z)$  for the mean and standard deviation, respectively. We then initialize Gaussian distributions -  $\mathcal{N}(\mu(x), \sigma^2(x))$ ,  $\mathcal{N}(\mu(y), \sigma^2(y))$ ,  $\mathcal{N}(\mu(z), \sigma^2(z))$ —and use these distributions to sample centroid locations for MS volumes in the head and neck MRI. It is worth noting that the mean and standard deviation of the left and right MS volumes are different, resulting in a total of six Gaussian distributions in practice. In practice, for the left MS the  $x$ ,  $y$  and  $z$   $\mu$  are 75, 231 and 121 mm and  $\sigma$  are 1.47, 1.56 and 1.76 mm, respectively. Correspondingly for the right MS, the  $x$ ,  $y$  and  $z$   $\mu$  are 149, 232 and 118 mm and  $\sigma$  are 1.90, 1.66 and 6.47 mm respectively. We sample  $N$  left MS volumes and  $N$  right MS from each head and neck MRI where  $N$  is the sample size. For our experiments,  $N \in \{1, 5, 10, 15, 20\}$ . An illustration of our sampling method is shown in Fig. 1a. We extract MS volumes of multiple sizes namely,  $25 \times 25 \times 25$ ,  $30 \times 30 \times 30$ ,  $35 \times 35 \times 35$ ,  $40 \times 40 \times 40$ ,  $45 \times 45 \times 45$ . The extracted MS volumes are finally resampled to a resolution of  $64 \times 64 \times 64$  for the 3D CNN. To make the right and left MS appear more symmetrical, we horizontally flip the coronal planes of the right MS to give it the appearance of the left MS volume. Figure 2 illustrates our data processing pipeline.

**Training, validation and test splits:** if we sample with  $N = 1$ , we end up with 327, 37 and 41 MS volumes in the training, validation and test set, respectively. The training validation and test set size increase by a factor of  $N$  with respect to the sample size  $N$ . 32% of the MS volumes in the training, validation and test sets are anomalous MS volumes. We perform threefold cross-validation experiments with all the methods.

**Fig. 1** **a** Illustration of our MS volume extraction strategy showing 3 MS volumes for left and right MS each. **b** Flipping of the coronal plane of the right MS. **c** Illustration of our MIE prediction strategy used during inference. GAP denotes Global Average Pooling and FC denotes Fully Connected Layer



**Implementation details** We implement a 3D CNN using ResNet18 [21] with four stages of 3D residual blocks (channel dimensions 64, 128, 256, 512). Our models are trained for 100 epochs with a batch size of 16, a learning rate of 0.0001, and Adam optimization. If the validation loss did not improve for 5 epochs, the learning rate is reduced by a factor of 10. We use PyTorch and PyTorch Lightning to build our models.

**DL method:** to classify the MS volume into normal or anomaly class, we consider multiple 3D ResNet [21]<sup>1</sup> and 3D DenseNet [22] architectures.<sup>2</sup> Let us denote the classifier as  $f(\cdot)$  and the MRIs as  $X \in R^{H \times W \times D}$ . From each MRI, we extract  $N$  left MS volumes and  $N$  right MS volumes. Alto-

gether, we extract  $2N$  MS volumes from  $X \in R^{H \times W \times D}$ . Let us denote the MS volumes as  $x \in R^{P \times P \times P}$ . Here,  $P$  denotes the size of the MS volume such that  $P \in \{25, 30, 35, 40, 45\}$ . Further, our labels  $y \in \{0, 1\}$  represent normal and anomaly class. The anomaly class is the positive class for our use-case. As a baseline, we consider 3DResNet models that do not use our MIE strategy for inferring on the test set.

**Multiple instance ensemble prediction strategy:** let us denote the extracted MS volumes from a single MRI  $x_i \in R^{P \times P \times P}$  where  $i$  denotes the  $i$ -th MS volume extracted from either the left or right MS area of the MRI. When making a prediction, we average the softmax scores of classifier  $f(\cdot)$  from the multiple MS volumes  $x_i$ . Formally,

$$\hat{y} = \frac{1}{N} \sum_{i=1}^N \text{softmax}(f(x_i))$$

<sup>1</sup> <https://github.com/kenshohara/3D-ResNets-PyTorch/blob/master/models/resnet.py>.

<sup>2</sup> <https://github.com/kenshohara/3D-ResNets-PyTorch/blob/master/models/densenet.py>.

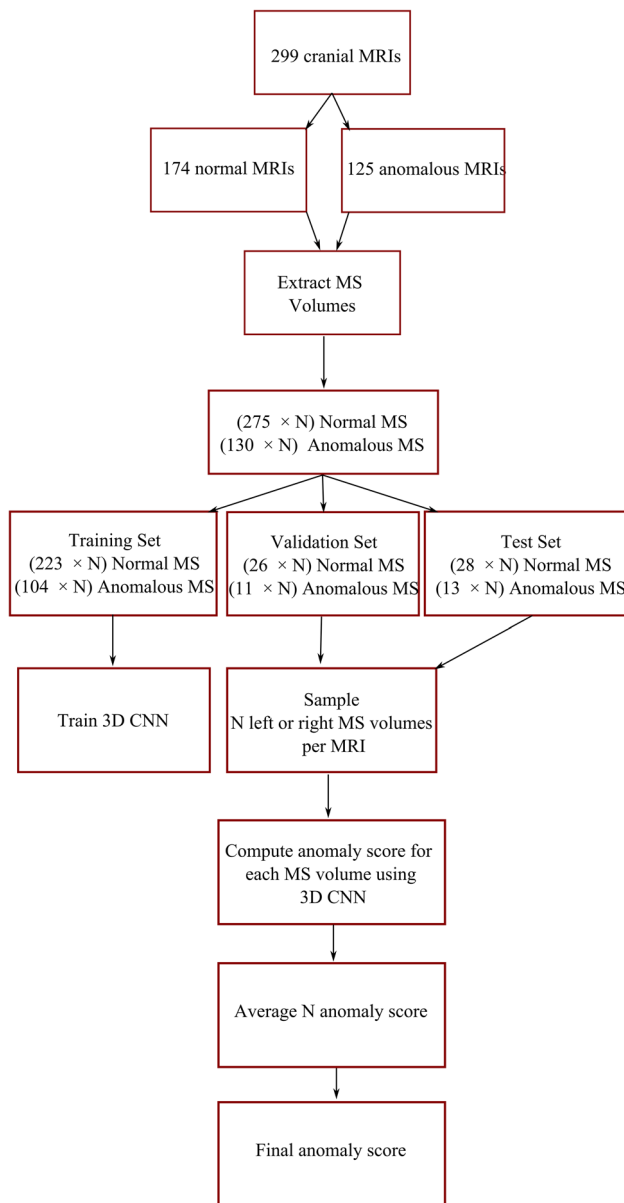


Fig. 2 Illustration of our data processing pipeline

## Results

### Effect of sampling size

We plot the mean and standard deviation of the Area Under Precision Recall Curve (AUPRC) and F1 score. Both these metrics are useful especially in imbalanced scenarios which is our case. From Table 1, we observe that with the increase in the sample size  $N$ , we get a consistent increase in all the reported metrics until  $N = 15$  after which we get a decrease in all the metrics. Further, for all the cases, we see that using MIE strategy is beneficial for MS anomaly classification and leads to boost in classification metrics.

### Comparison with state-of-the-art 3D CNN architectures

We investigate the benefits of sampling and ensembling techniques on 3D CNN architectures for medical imaging classification. Specifically, we examine their impact on 3D DenseNet and 3D ResNets used in various medical imaging tasks [23–28]. Using  $N = 15$ , we conduct an ablation study, training the CNNs with sampled data but inferring with a single MS volume. We observe that, for ResNets, the AUPRC decreases as architecture complexity increases, but with  $N=15$  and MIE enabled, the decrease is minimal. Sampling and sampling with MIE consistently improve performance for both ResNets and DenseNets, resulting in percentage increases of  $21.86 \pm 11.92\%$  and  $4.27 \pm 5.04\%$  (sampling) and  $28.86 \pm 12.80\%$  and  $9.85 \pm 4.02\%$  (sampling + MIE) in AUPRC, respectively

### Effect of sampling type

In our methods, we adopt a Gaussian distribution to model centroid locations and sample random centroids for extracting corresponding MS volumes. However, an alternative approach is to extract equidistant centroids, which allows us to investigate potential advantages of random sampling. For this experiment, we consider the  $x$ ,  $y$ , and  $z$  coordinates of the centroid to lie on lines starting at  $\mu(x) - \sigma(x)$ ,  $\mu(y) - \sigma(y)$  and  $\mu(z) - \sigma(z)$ , respectively, and ending at  $\mu(x) + \sigma(x)$ ,  $\mu(y) + \sigma(y)$  and  $\mu(z) + \sigma(z)$ . Figure 3 illustrates the relationship between these axes and the MRI image from which the coordinates are sampled. Utilizing these lines, we sample  $N$  equidistant centroid locations, while also exploring variations such as fixing one or two coordinates at their means. Referred to as *equidistant sampling*, we compare this strategy and its variants against the random sampling method we propose. Table 3 presents our findings, demonstrating the most advantageous sampling from the  $z$ -axis for classification. Equidistant sampling from all axes yields an AUPRC of  $0.89 \pm 0.03$ , while equidistant sampling from  $x$  and  $y$  axes with a constant  $z$  coordinate results in an AUPRC of  $0.82 \pm 0.16$ , showcasing an 8.18% difference. Similarly, fixing the  $y$ -coordinate incurs a 1.12% AUPRC decrease, while maintaining a constant  $z$ -coordinate exhibits no AUPRC decrease. These results suggest varying importance in sampling MS centroid coordinates from each axis, with random sampling proving to be the most effective approach.

### Effect of patch size

Further, looking at Fig. 4, we can see the influence of MS volume size to the paranasal classification task. Note, we set  $N = 15$  for this experiment and use our multiple instance ensemble prediction strategy. This highlights that patch size

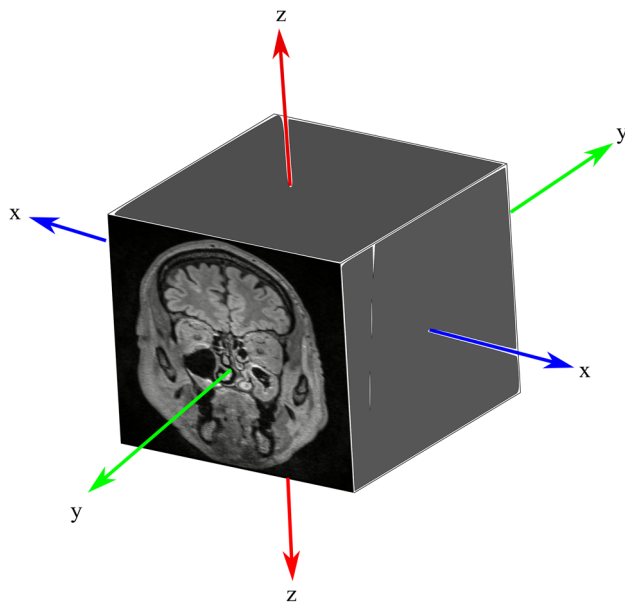


**Fig. 3**  $x$ ,  $y$  and  $z$  axis for an MRI

**Table 1** Result of our experiments

$N$	MIE	AUPRC	F1
1		$0.80 \pm 0.12$	$0.70 \pm 0.13$
5		$0.85 \pm 0.03$	$0.77 \pm 0.10$
5	✓	$0.87 \pm 0.04$	$0.76 \pm 0.10$
10		$0.85 \pm 0.04$	$0.75 \pm 0.08$
10	✓	$0.89 \pm 0.05$	$0.79 \pm 0.10$
15		$0.88 \pm 0.07$	$0.81 \pm 0.12$
15	✓	<b><math>0.92 \pm 0.06</math></b>	<b><math>0.85 \pm 0.09</math></b>
20		$0.87 \pm 0.04$	$0.77 \pm 0.05$
20	✓	$0.91 \pm 0.02$	$0.78 \pm 0.07$

Patch size  $P = 35$  for all the experiments and 3D ResNet18 architecture used

The bold signifies the highest/best metric in each column of a table

**Table 2** Result of our experiments

CNN	N	MIE	AUPRC	F1
3D ResNet18	1		$0.80 \pm 0.12$	$0.70 \pm 0.13$
3D ResNet18	15		$0.88 \pm 0.07$	$0.81 \pm 0.12$
3D ResNet18	15	✓	$0.92 \pm 0.06$	$0.85 \pm 0.09$
3D ResNet50	1		$0.72 \pm 0.13$	$0.59 \pm 0.19$
3D ResNet50	15		$0.82 \pm 0.11$	$0.71 \pm 0.19$
3D ResNet50	15	✓	$0.85 \pm 0.07$	$0.74 \pm 0.13$
3D ResNet101	1		$0.73 \pm 0.10$	$0.59 \pm 0.04$
3D ResNet101	15		$0.85 \pm 0.04$	$0.69 \pm 0.10$
3D ResNet101	15	✓	$0.90 \pm 0.06$	$0.79 \pm 0.14$
3D ResNet152	1		$0.66 \pm 0.06$	$0.57 \pm 0.08$
3D ResNet152	15		$0.83 \pm 0.07$	$0.76 \pm 0.11$
3D ResNet152	15	✓	$0.89 \pm 0.05$	$0.80 \pm 0.08$
3D ResNet200	1		$0.60 \pm 0.21$	$0.45 \pm 0.39$
3D ResNet200	15		$0.86 \pm 0.05$	$0.79 \pm 0.10$
3D ResNet200	15	✓	$0.90 \pm 0.04$	$0.83 \pm 0.07$
3D DenseNet121	1		$0.86 \pm 0.11$	$0.80 \pm 0.07$
3D DenseNet121	15		$0.86 \pm 0.10$	$0.81 \pm 0.06$
3D DenseNet121	15	✓	$0.92 \pm 0.05$	$0.83 \pm 0.12$
3D DenseNet169	1		$0.81 \pm 0.09$	$0.76 \pm 0.11$
3D DenseNet169	15		$0.91 \pm 0.05$	$0.82 \pm 0.04$
3D DenseNet169	15	✓	$0.94 \pm 0.03$	$0.86 \pm 0.09$
3D DenseNet201	1		$0.88 \pm 0.07$	$0.72 \pm 0.07$
3D DenseNet201	15		$0.88 \pm 0.04$	$0.72 \pm 0.08$
3D DenseNet201	15	✓	$0.93 \pm 0.06$	$0.78 \pm 0.07$
3D DenseNet264	1		$0.84 \pm 0.09$	$0.81 \pm 0.07$
3D DenseNet264	15		$0.88 \pm 0.05$	$0.82 \pm 0.12$
3D DenseNet264	15	✓	$0.93 \pm 0.01$	$0.85 \pm 0.09$

Patch size  $P = 35$  for all the experiments

plays an important role in boosting the paranasal anomaly classification performance. Our experiments indicate that the optimal patch size for our dataset is  $P = 35$ .

**Table 3** Experiment on sampling strategy

$x$	$y$	$z$	AUPRC	F1
$\mu(x)$	$\mu(y) \pm \sigma(y)$	$\mu(z) \pm \sigma(z)$	$0.89 \pm 0.03$	$0.74 \pm 0.03$
$\mu(x) \pm \sigma(x)$	$\mu(y)$	$\mu(z) \pm \sigma(z)$	$0.88 \pm 0.04$	$0.77 \pm 0.04$
$\mu(x) \pm \sigma(x)$	$\mu(y) \pm \sigma(y)$	$\mu(z)$	$0.82 \pm 0.16$	$0.73 \pm 0.19$
$\mu(x)$	$\mu(y)$	$\mu(z) \pm \sigma(z)$	$0.89 \pm 0.03$	$0.77 \pm 0.04$
$\mu(x)$	$\mu(y) \pm \sigma(y)$	$\mu(z)$	$0.85 \pm 0.08$	$0.68 \pm 0.18$
$\mu(x) \pm \sigma(x)$	$\mu(y)$	$\mu(z)$	$0.85 \pm 0.04$	$0.75 \pm 0.03$
$\mu(x) \pm \sigma(x)$	$\mu(y) \pm \sigma(y)$	$\mu(z) \pm \sigma(z)$	$0.89 \pm 0.03$	$0.79 \pm 0.06$
$\mathcal{N}(\mu(x), \sigma^2(x))$	$\mathcal{N}(\mu(y), \sigma^2(y))$	$\mathcal{N}(\mu(z), \sigma^2(z))$	<b><math>0.92 \pm 0.07</math></b>	<b><math>0.85 \pm 0.09</math></b>

Patch size  $P = 35$  for all the experiments.  $\mu \pm \sigma$  represents equidistant sampling of  $N$  points from a line starting at  $\mu - \sigma$  and ending at  $\mu + \sigma$ .  $\mathcal{N}(\mu, \sigma^2)$  represents random sampling of points from a Gaussian distribution parameterized by  $\mu$  and  $\sigma$ . 3D ResNet18 architecture used



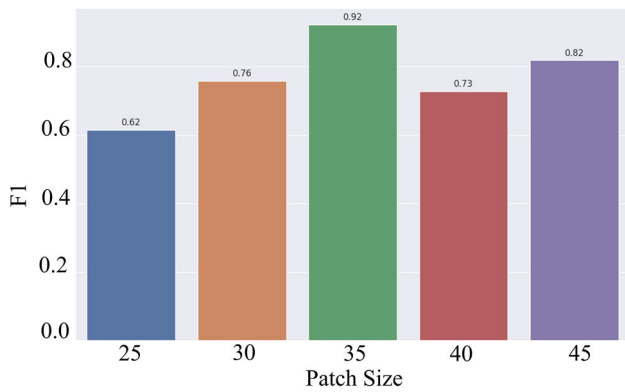


**Fig. 4** F1 scores vs patch size  $P$

## Discussion

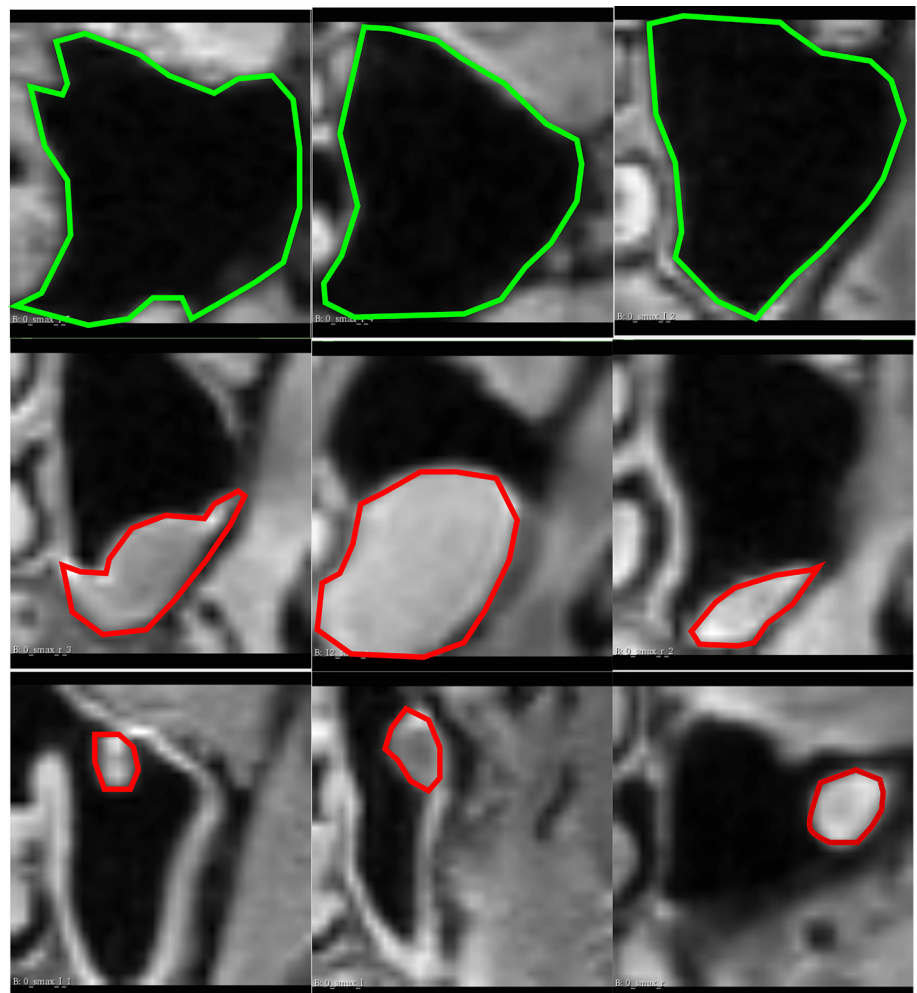
Clinicians classifying paranasal anomalies face the burdensome task of manually searching for MS-containing slices in MRI sequences and then diagnosing, resulting in time-consuming and fatiguing analysis. Additionally, the task of

classifying paranasal anomalies is challenging due to the morphological variation of the maxillary sinus as well as the polyp and cyst anomalies inhabiting the sinuses. This can be seen in Fig. 5. Previous approaches [18] used a 2-stage CNN pipeline, learning key MS slices first using a CNN and then classifying anomalies with another CNN [18] or learning to segment the maxillary sinus and then classifying the anomaly [17], but these methods 2 stage CNN pipeline makes it dependent on datasets hindering generalization. To overcome this limitation, we propose a method that extracts multiple MS volumes without DL, using a CNN only once to compute the final anomaly score for each MS. This streamlined approach reduces dataset dependency and facilitates broader applicability to other modalities.

As seen in Table 1, increasing the sample size  $N$  improves classification metrics, but a sample size of 20 exhibits a lower F1 score compared to 15, possibly due to overfitting caused by redundant volumes. Thus, careful selection of the appropriate sample size is crucial for optimal performance.

We compared different CNN architectures in Table 2 and found that sampling and MIE are beneficial for our

**Fig. 5** The coronal planes of the sampled MS volumes. The green contours in the first row represent normal MS anatomy. The red contours enclose masses that represent cysts and polyps in the second and third row, respectively, demonstrating the variety of appearances and morphological variations of these anomalies within the MS



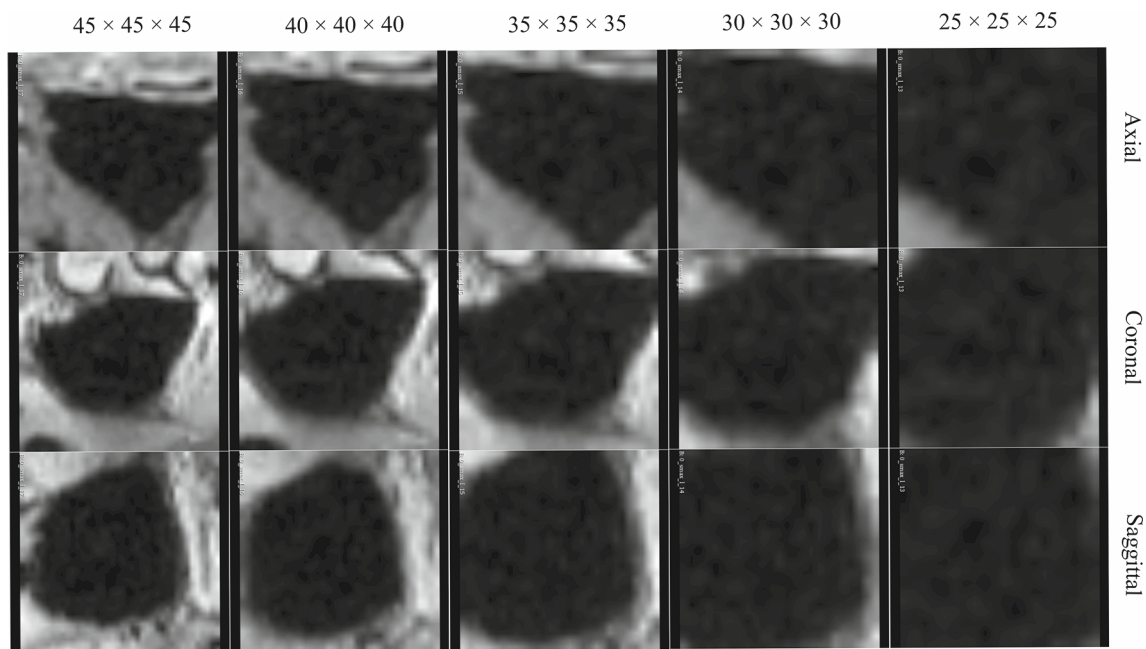


**Fig. 6** Slices from the axial, coronal and sagittal slices of extracted healthy MS volume with different patch sizes

classification task. The advantages of MIE and sampling are more prominent in ResNet architectures compared to DenseNet. We hypothesize that the multiple skip connections in a dense block [29] contribute to improved gradient flow and optimization in the  $N = 1$  sampling scenario. Our method consistently increases AUPRC, with sampling + MIE showing higher efficacy than only sampling and no sampling, demonstrating the effectiveness of our approach.

We compared random sampling and equidistant sampling's impact on classification performance in Table 3. Random sampling yielded better results, likely due to the diverse multi-scale volumes obtained through randomization. Equidistant sampling along the  $z$ -axis significantly improved classification performance, possibly due to higher  $z$ -coordinate  $\sigma$ , resulting in greater spatial offsets. This increased diversity in sampled volumes facilitated better feature learning and classification performance. Incorporating multi-scale volumes from different  $z$ -axis positions enhanced the ability of our 3D CNN to identify patterns, improving overall performance.

Additionally, using an ensemble strategy that averages the scores from multiple instances of the MS leads to a further improvement in classification metrics. The improvement in our classification metrics can be attributed to the incorporation of implicit test-time augmentation during inference on the test set. By sampling multiple overlapping MS volumes, we have MS volumes which have transnational offsets with respect to one another, resulting in better performance. These findings demonstrate the utility of our proposed method for the classification of paranasal anomalies in the MS.

The size of the extracted MS volume is critical for accurate classification. Small volumes may miss important details, while large volumes include irrelevant information as can be seen in Fig. 6. Our evaluation of different sizes ( $25 \times 25 \times 25$  to  $45 \times 45 \times 45$ ) found that  $35 \times 35 \times 35$  yielded the highest F1 score. This suggests that small volumes miss anomalies, while larger volumes include unnecessary structures. Careful selection of the patch size is crucial for optimal performance.

## Conclusion

We propose a DL approach for classifying maxillary sinus anomalies. Our method employs multiple instance ensemble prediction and a sampling strategy to improve classification performance on available dataset. We investigate the optimal sample size and patch size trade-off. Although further improvements are needed for real-world clinical use, our work offers a promising solution for maxillary sinus anomaly classification with DL.

**Acknowledgements** This work has not been submitted for publication anywhere else. This work is funded partially by the i3 initiative of the Hamburg University of Technology. The authors also acknowledge the partial funding by the Free and Hanseatic City of Hamburg (Interdisciplinary Graduate School) from University Medical Center Hamburg-Eppendorf. This work was partially funded by Grant Number KK5208101KS0 (Zentrales Innovationsprogramm Mittelstand, Arbeitsgemeinschaft industrieller Forschungsvereinigungen).

**Funding** Open Access funding enabled and organized by Projekt DEAL.

## Declarations

**Conflict of interest** Debayan Bhattacharya states no conflict of interest. Finn Behrendt states no conflict of interest. Benjamin Tobias Becker states no conflict of interest. Dirk Beyersdorff states no conflict of interest. Elina Petersen states no conflict of interest. Marvin Petersen states no conflict of interest. Bastian Cheng states no conflict of interest. Dennis Eggert states no conflict of interest. Christian Betz states no conflict of interest. Anna Sophie Hoffmann states no conflict of interest. Alexander Schlaefer states no conflict of interest.

**Ethical approval** The study protocol received approval from the local ethics committee (Landesärztekammer Hamburg, PV5131) and was approved by the Data Protection Commissioners for the University Medical Center of the University Hamburg-Eppendorf and the Free and Hanseatic City of Hamburg. It is registered on ClinicalTrials.gov (NCT03934957) and adheres to Good Clinical Practice, Good Epidemiological Practice, and ethical principles outlined in the Declaration of Helsinki.

**Open Access** This article is licensed under a Creative Commons Attribution 4.0 International License, which permits use, sharing, adaptation, distribution and reproduction in any medium or format, as long as you give appropriate credit to the original author(s) and the source, provide a link to the Creative Commons licence, and indicate if changes were made. The images or other third party material in this article are included in the article's Creative Commons licence, unless indicated otherwise in a credit line to the material. If material is not included in the article's Creative Commons licence and your intended use is not permitted by statutory regulation or exceeds the permitted use, you will need to obtain permission directly from the copyright holder. To view a copy of this licence, visit <http://creativecommons.org/licenses/by/4.0/>.

## References

- Martini, F., Timmons, M.J., Tallitsch, R.B.: Human anatomy. 6th edn. San Francisco, Pearson Benjamin Cummings (2009)
- Bal M, Berkiten G, Uyanik E (2014) Mucous retention cysts of the paranasal sinuses. *Hippokratia* 18(4):379
- Varshney H, Varshney J, Biswas S, Ghosh SK (2015) Importance of CT scan of paranasal sinuses in the evaluation of the anatomical findings in patients suffering from sinonasal polyposis. *Indian J Otolaryngol Head Neck Surg* 68(2):167–172
- Hansen AG, Helvik A-S, Nordgård S, Bugten V, Stovner LJ, Håberg AK, Gårseth M, Eggesbø HB (2014) Incidental findings in MRI of the paranasal sinuses in adults: a population-based study (hunt MRI). *BMC Ear, Nose, and Throat Disord* 14(1):13. <https://doi.org/10.1186/1472-6815-14-13>
- Tarp B, Fiirgaard B, Christensen T, Jensen JJ, Black FT (2000) The prevalence and significance of incidental paranasal sinus abnormalities on MRI. *Rhinology* 38(1):33–38
- Rak KM, Newell JD, Yakes WF, Damiano MA, Luethke JM (1991) Paranasal sinuses on MR images of the brain: significance of mucosal thickening. *AJR Am J Roentgenol* 156(2):381–384. <https://doi.org/10.2214/ajr.156.2.1898819>
- Stenner M, Rudack C (2014) Diseases of the nose and paranasal sinuses in child. *GMS Curr Top Otorhinolaryngol, Head Neck Surg* 13:10. <https://doi.org/10.3205/cto000113>
- Rege ICC, Sousa TO, Leles CR, Mendonça EF (2012) Occurrence of maxillary sinus abnormalities detected by cone beam CT in asymptomatic patients. *BMC Oral Health* 12:30. <https://doi.org/10.1186/1472-6831-12-30>
- Cooke LD, Hadley DM (1991) MRI of the paranasal sinuses: incidental abnormalities and their relationship to symptoms. *J Laryngol Otol* 105(4):278–281. <https://doi.org/10.1017/s0022215100115609>
- Brierley J, Gospodarowicz MK, Wittekind C (eds) (2017) TNM classification of malignant tumours, 8th edn. Wiley, Chichester, West Sussex, Hoboken
- Gutmann A (2013) Ethics. The bioethics commission on incidental findings. *Science (New York)* 342(6164):1321–1323. <https://doi.org/10.1126/science.1248764>
- Ma Z, Yang X (2012) Research on misdiagnosis of space occupying lesions in unilateral nasal sinus. *Lin chuang er bi yan hou tou jing wai ke za zhi = J Clin Otorhinolaryngol, Head, Neck Surg* 26(2):59–61. <https://doi.org/10.13201/j.issn.1001-1781.2012.02.005>
- Papadopoulou A-M, Chrysikos D, Samolis A, Tsakotos G, Troupis T (2021) Anatomical variations of the nasal cavities and paranasal sinuses: a systematic review. *Cureus* 13(1):12727
- Mohindru V, Singla S (2021) A review of anomaly detection techniques using computer vision. In: Singh PK, Singh Y, Kolekar MH, Kar AK, Chhabra JK, Sen A (eds) Recent innovations in computing. Springer, Singapore, pp 669–677
- Tschuchnig ME, Gadermayr M (2022) Anomaly detection in medical imaging—a mini review. In: Haber P, Lampoltshammer TJ, Leopold H, Mayr M (eds) Data Sci-Analyt Appl. Springer, Wiesbaden, pp 33–38
- Kim HG, Lee KM, Kim EJ, Lee JS (2019) Improvement diagnostic accuracy of sinusitis recognition in paranasal sinus X-ray using multiple deep learning models. *Quant Imaging Med Surg* 9:942–951. <https://doi.org/10.21037/QIMS.2019.05.15>
- Ozbay S, Tunc O (2022) Deep learning in analysing paranasal sinuses. *Elektron Elektrotech* 28:65–70. <https://doi.org/10.5755/J02.EIE.31133>
- Kim K-S, Kim BK, Chung MJ, Cho HB, Cho BH, Jung YG (2022) Detection of maxillary sinus fungal ball via 3-d CNN-based artificial intelligence: fully automated system and clinical validation. *PLoS One* 17(2):1–19. <https://doi.org/10.1371/journal.pone.0263125>
- Jagodzinski A, Blankenberg S et al (2020) Rationale and design of the Hamburg city health study. *Eur J Epidemiol* 35(2):169–181. <https://doi.org/10.1007/s10654-019-00577-4>
- Garyfallidis E, Brett M, Amirbekian B, Rokem A, van der Walt S, Descoteaux M, Nimmo-Smith I (2014) Dipy, a library for the analysis of diffusion MRI data. *Front Neuroinform* 8:8. <https://doi.org/10.3389/FNINF.2014.00008/BIBTEX>
- Hara, K., Kataoka, H., Satoh, Y.: Learning spatio-temporal features with 3D residual networks for action recognition. [arXiv:1708.07632v1](https://arxiv.org/abs/1708.07632v1)
- Fu J, Singhrao K, Qi XS, Yang Y, Ruan D, Lewis JH (2021) Three-dimensional multipath densenet for improving automatic segmentation of glioblastoma on pre-operative multimodal MR images. *Med Phys* 48(6):2859–2866. <https://doi.org/10.1002/mp.14800>
- Zhang, G., Lin, L., Wang, J.: Lung nodule classification in ct images using 3d densenet. *Journal of Physics: Conference Series* 1827 (2021)
- Liu Z, Zhu Y, Yuan Y, Yang L, Wang K, Wang M, Yang X, Wu X, Tian X, Zhang R, Shen B, Luo H, Feng H, Feng S, Ke Z (2021) 3D DenseNet deep learning based preoperative computed tomography for detecting myasthenia gravis in patients with thymoma. *Front Oncol* 11:631964
- Näppi, J.J., Hironaka, T., Yoshida, H.: Detection of colorectal masses in CT colonography: application of deep residual networks



- for differentiating masses from normal colon anatomy. In: Medical Imaging (2018)
26. Chen, X., Wang, Z., Zhan, Y., Cheikh, F.A., Ullah, M.: Interpretable learning approaches in structural MRI: 3d-resnet fused attention for autism spectrum disorder classification. In: Medical Imaging (2022)
27. Suryakanth, B., Hari Prasad, S.A.: 3D CNN-residual neural network based multimodal medical image classification. *Int J Eng Trends Technol* **70**(10), 371–380 (2022). <https://doi.org/10.14445/22315381/IJETT-V70I10P236>
28. Uemura, T., Näppi, J.J., Hironaka, T., Kim, H., Yoshida, H.: Comparative performance of 3d-densenet, 3d-resnet, and 3d-vgg models in polyp detection for CT colonography. In: Medical Imaging (2020)
29. Huang, G., Liu, Z., Maaten, L.V.D., Weinberger, K.Q.: Densely connected convolutional networks. In: 2017 IEEE Conference on Computer Vision and Pattern Recognition (CVPR), pp. 2261–2269. IEEE Computer Society, Los Alamitos (2017). <https://doi.org/10.1109/CVPR.2017.243>

**Publisher's Note** Springer Nature remains neutral with regard to jurisdictional claims in published maps and institutional affiliations.